Convergence in the Evolution of Nanodiamond Raman Spectra with Particle Size: A Theoretical Investigation

Wunfan Li,[†,‡] Stephan Irle,[‡,*] and Henryk A. Witek[†,*]

[†]Institute of Molecular Science and Department of Applied Chemistry, National Chiao Tung University, Hsinchu, Taiwan, and [‡]Institute for Advanced Research and Department of Chemistry, Nagoya University, Nagoya 464-8602, Japan

ABSTRACT Structural characterization of nanodiamonds by vibrational spectroscopy requires knowledge of the factors determining the spectra. Raman spectroscopy is widely used to detect the diamond phase in nanodiamond powders and films, but several spectral features are still poorly understood. Here we present a theoretical study of the evolution of diamond hydrocarbon Raman spectra with increasing size, from the adamantane molecule to ~3 nm large tetrahedral and octahedral particles of T_d symmetry, containing up to about 1000 carbon atoms. The self-consistent-charge density functional tight-binding method (SCC-DFTB) was used for the calculation of harmonic first-order Raman spectra. We demonstrate very good agreement with Raman spectra computed by standard density functional theory (DFT) for the smaller model systems. The evolution of the Raman patterns is smooth, and convergence to the bulk limit could clearly be observed in case of the acoustic vibrational modes ($\omega_A = 0$ cm^{-1}). We found a simple relationship between nanodiamond size and vibrational frequency, which is analogous to the corresponding equation for the radial breathing mode of single-walled carbon nanotubes. The T_2 modes of octahedral diamond hydrocarbons coalesce faster to the bulk optical vibrational mode (in experiment, $\omega_0 = 1332$ cm^{-1}) than those of tetrahedral particles, consistent with the fact that the bulk/surface ratio is more favorable for octahedral particles. Our simulations unequivocally show that controversial Raman features around 500 and 1150 cm^{-1} do not originate from the nanodiamond crystals, and that the nanocrystal shape plays an important role in the appearance of the Raman spectra even in the 3 nm domain.

KEYWORDS: Raman intensities · vibrational spectroscopy · nanodiamonds · density functional tight binding · size evolution of Raman spectra

Nanometer-sized diamond is an unusual form of carbon that has been observed in interstellar dust and meteorites.[1,3] The detonation synthesis of nanodiamond (ND) was discovered in the 1960s,[2] but nowadays, nanocrystalline diamond films are often grown by chemical vapor decomposition (CVD) methods from activated diluted hydrocarbon−hydrogen gas mixtures.[4] Their physicochemical properties are hoped to become controllable by size- and shape-specific CVD synthesis, while already a variety of potential commercial ND applications were already reported during the past few years using the rather crude detonation synthesis.[5−9] Due to their inherent biocompatibility, NDs have recently been "discovered" for medical applications,[10] for instance, for drug delivery[11,12] and biolabeling.[13,14] In this context, use is made of surface or subsurface dopant species[13,14] or surface functionalization.[11,12]

Structural characterization of NDs by means of spectroscopic techniques is of critical importance for the further development of the ND research field, as well as for practical applications. For this purpose, a thorough understanding of the factors affecting the spectroscopic properties is urgently required. Among the possible spectroscopic techniques, Raman vibrational spectroscopy has become one of the most valuable tools used for the structural characterization of NDs[15−25] and their structural transformations at high temperatures.[26] A number of characteristic features were proposed to discriminate NDs from other carbon nanomaterials. These features—Raman active bands that show up in spectra of nanocrystalline diamond in addition to the characteristic diamond signal (which is broadened and slightly red-shifted from its bulk value of 1332 cm^{-1})—include the bands around 500, 600, 1150, 1400, 1450, and 1500−1800 cm^{-1}.[15−19,25] However, serious controversies exist preventing an unequivocal assignment of the observed vibrational bands to NDs, and it is far from clear whether these bands can be attributed to the NDs themselves.[19−21] There is now a consensus that the peak around 1150 cm^{-1}, which always appears together with the peak at 1450 cm^{-1} in poor quality CVD-synthesized NDs, originates from *trans*-polyacetylene fragments.[19,25] The origin of the double-resonant band at 1400 cm^{-1} and that of the broad asymmetric peak between 1500 and 1800 cm^{-1} has been ascribed to D- and G-bands of graphitic surface species, but in the case of the peak labeled as "G-band", it was recently shown that it is composed of O−H bending with

*Address correspondence to sirle@iar.nagoya-u.ac.jp, hwitek@mail.nctu.edu.tw.

Received for review March 2, 2010 and accepted July 06, 2010.

Published online July 19, 2010. 10.1021/nn1004205

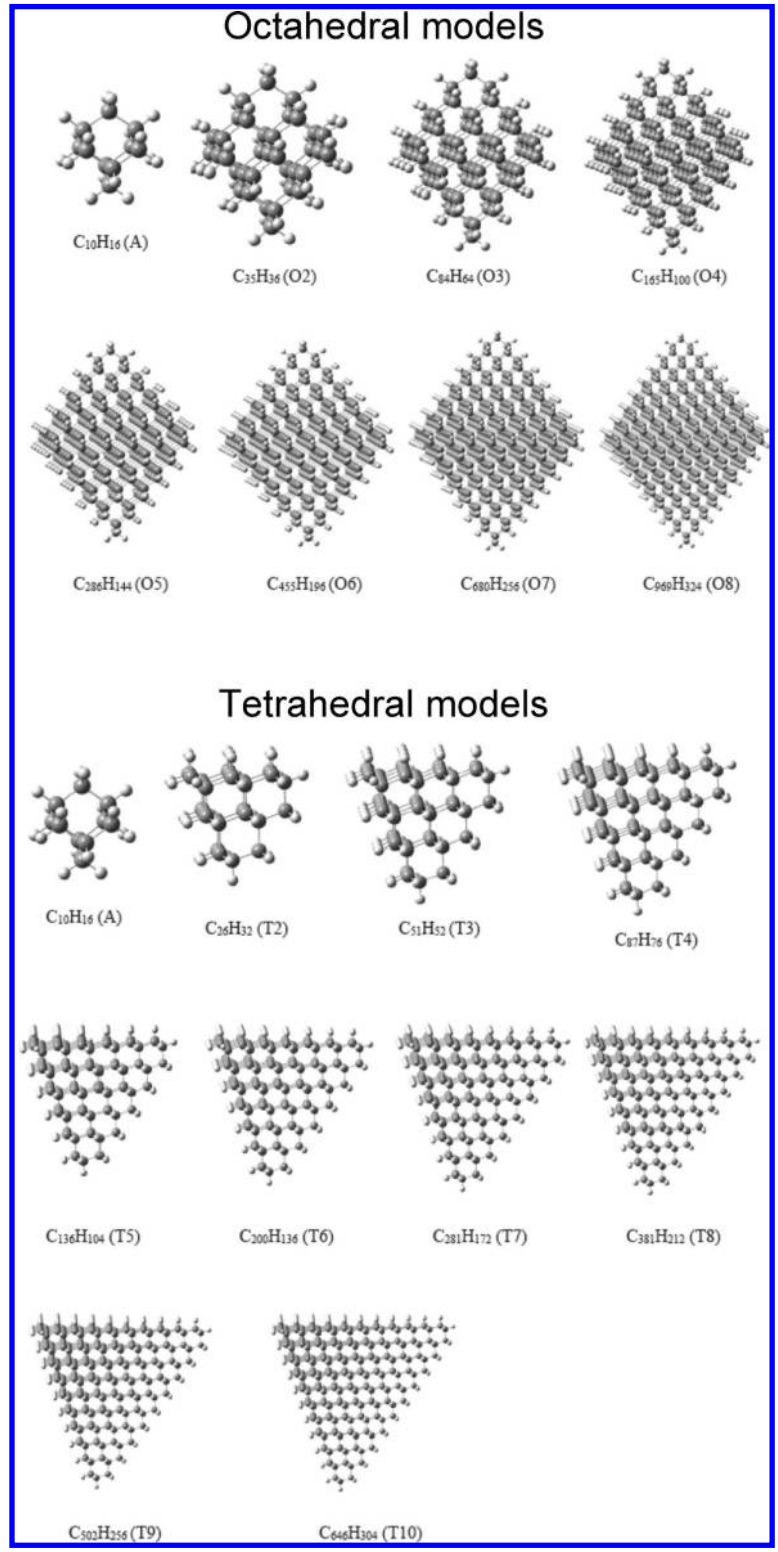

Figure 1. Molecular structures and formulas of the octahedral (A, O2−O8) and tetrahedral (A, T2−T10) ND models considered in the present study.

contributions from sp^2 carbon and C═O stretching vibrations.[25]

Theoretical calculations of Raman spectra based on (scaled) harmonic vibrational frequencies are often performed for the assignment of experimental spectra. In the case of NDs, only two density functional theory (DFT) and Hartree−Fock (HF)-based studies have been published previously,[27,28] which reported contradictory conclusions regarding the peak assignments. Zhang and Zhang—using rather tiny molecular models of nanodiamonds up to the size of 44 carbon atoms—predicted[27] that only the band at ~500 cm^{-1}

should be indicative of the presence of nanodiamonds, while the other experimental bands around 1140 and 1480 cm^{-1} were ascribed to Raman activity of sp^2-bonded carbon atoms. Filik *et al.*—using slightly larger models up to 88 carbon atoms—argued[28] that actually none of these features originate from nanodiamonds, suggesting that the only Raman activity of NDs is produced by the broadened zone-center (1325 cm^{-1}) mode and low-frequency (<100 cm^{-1}) cage deformation modes. The authors conceded that their small model systems were not sufficiently large enough to make definite assignments of the experimental bands appearing in ND Raman spectra. A thorough theoretical study of the evolution of Raman spectra from adamantane to bulk diamond was considered impossible.[27−29]

The calculation of Raman spectra by standard *ab initio* or first-principles methods requires enormous computational resources, imposing severe restrictions on these conventional quantum chemical methods. Yet, the high density of diamond requires the use of model systems with a large number of atoms in even moderate-size atomistic model systems. We have shown in recent studies that the computationally much more economical self-consistent-charge density functional tight-binding (SCC-DFTB, abbreviated in the following text as DFTB) method[30,31] is comparable in accuracy to conventional DFT methods for the theoretical investigation of vibrational IR and Raman spectra[32,33] and can easily surpass the size limitations imposed on the first-principles methods.[34−37] DFTB is therefore ideally suited for a study of the size and shape effect on the theoretical Raman spectra of finite-size atomistic model systems for ND species and in the position to shed light on the discrepancies between the previously published studies.

In this work, we focus on the size evolution of the Raman bands of nanocrystalline diamonds using two families (tetrahedral and octahedral) of finite molecular models. We selected these two families because they represent examples of least and higher sphericity of shape; NDs synthesized or found in nature certainly come in a great variety of shapes, most prominently quasi-spherical, but also irregular shapes with no symmetry at all. The simulated spectra can be expected to converge to the extremely simple Raman spectrum of bulk diamond, which consists of a single sharp peak at 1332 cm^{-1}. We note that vibrational analysis based on harmonic force constant approximation is not expected to yield the fundamental vibrational frequencies. Moreover, the limitations in the accuracy of quantum chemical methods for predicting harmonic force constants can lead to deviations up to the order of 100 cm^{-1}. The Raman spectra of nanocrystalline diamonds are, of course, more complex and depend strongly on the size and shape of the crystallite. In comparison with previous theoretical studies focusing on the simulation of Raman spectra, significantly larger molecular models of NDs are used—up to ~10^3 carbon atoms—which enable us to visualize the Raman spectrum evolution during the transition from the molecular to the solid-state regime. It is also shown here that a large portion of the simulated Raman signal is generated by the atoms located in the vicinity of the outer surface of the clusters. An attempt to eliminate the surface effects by immobilizing the terminal atoms shows that the convergence of the Raman spectra toward that of the bulk diamond is remarkably enhanced by this procedure.

Model Systems. The model systems employed in the present study were constructed taking into account the following symmetry considerations. The symmetry space group of the diamond crystal is *Fd3m*, and the corresponding point group is O_h. Some of the symmetry elements of O_h, like inversion center, are present only in infinite diamond crystals. The highest symmetry point group appropriate for finite molecules is T_d. Under the restriction of T_d symmetry, two different families of nanodiamond structures are conceivable: octahedral and tetrahedral. The building block used to construct these structures—adamantane ($C_{10}H_{16}$) referred to in the following as A—is identical for both families. By replicating the carbon backbone of the building block an appropriate number of times, we obtain seven octahedral (O2−O8) and nine tetrahedral (T2−T10) nanodiamond structures. Their molecular structures and chemical formulas are given in Figure 1. The outer surface of all of the models is saturated with hydrogen atoms. The largest considered structure (O8) consists of 969 carbon atoms. The size of the investigated models ranges from 0.3 nm (A) to 2.6 nm (T10) and 2.9 nm (O8) across the maximal carbon−carbon distance (r_{max}). It is convenient to give here an equation allowing an estimate for the size of the model structures from the number of the carbon atoms and *vice versa*. It was obtained by fitting r_{max} to the corresponding number of carbon atoms (n) for the five largest structures of each family. The correlation coefficient was practically equal to unity. The effective formula is given by

$$r_{max} = an^b - c \quad (1)$$

where a = 3.264 Å, b = 0.3349, and c = 3.5 Å for the octahedral models and a = 3.168 Å, b = 0.3498, and c = 4.5 Å for the tetrahedral models. As expected, the size of the models scales approximately as a cubic root of n.

RESULTS AND DISCUSSION

Comparison of DFTB with DFT and Previous Results. Both DFTB and DFT methods were used to compute Raman spectra of smaller model systems (A, T2−T4, O2, and O3), while for larger models (T5−T10 and O4−O8), only the DFTB method could be employed. To assess the quality of the DFTB Raman spectra, a comparison of the DFTB and DFT (BLYP/3-21G and BLYP/6-31+G*) Ra-

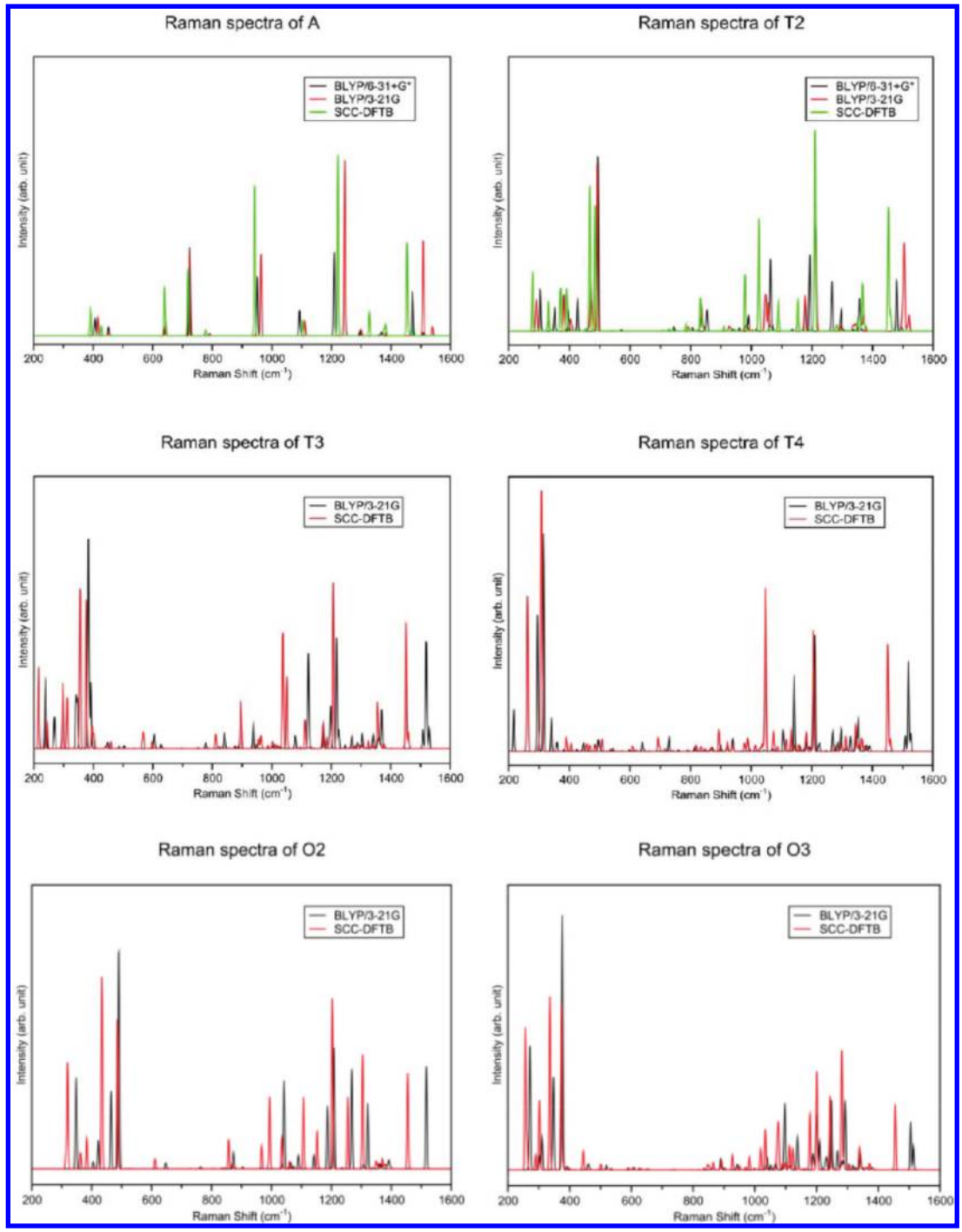

Figure 2. Comparison of the Raman spectra calculated using BLYP/3-21G, BLYP/6-31G*, and SCC-DFTB for the A, T2, T3, T4, O2, and O3 models.

man spectra computed for the smaller models is given in Figure 2. The overall agreement is satisfactory, with the largest discrepancies concerning a somewhat altered intensity pattern and shifts (up to 50 cm^{-1}) in the position of some of the peaks. This picture is consistent with our previous studies of the SCC-DFTB Raman spectra of organic molecules and fullerenes.[32,34,38] In the present study, the main differences between the spectra are associated with the vibrational activity of the CH_2 groups at the model system vertices, which, fortunately, is irrelevant for the main purpose of our current investigation. It was earlier demonstrated by Filik *et al.*[28] that a similar degree of change in the simulated Raman spectrum of adamantane can be induced upon the change of the computational method (HF *vs* DFT) and/or the basis set.

The previous theoretical studies of nanodiamond Raman spectra[27,28] were limited to very small molecular models with less than 100 atoms. The largest structure studied by Zhang and Zhang[27] ($C_{44}H_{42}$) is interme-

diate between our O2 and O3 models. Our simulated O2 spectrum agrees reasonably well with the O2 spectrum computed by these authors, who used a different level of DFT, namely, B3LYP/6-31G*. The largest atomistic models used by Filik *et al.*[28] comprise approximately 90 carbon atoms and are directly related to our O3 and T4 models. Unfortunately, it is not feasible to compare their Raman spectra with ours because they used Raman activities to display their data instead of more appropriate Raman intensities.

General Evolution of Raman Spectra of Octahedral and Tetrahedral NDs. Before presenting the results for the evolution of ND Raman spectra with increasing model system size, we shortly discuss the Raman spectrum of infinitely large diamond, which constitutes the bulk limit toward which our finite ND models are expected to converge. The phonon dispersion structure of diamond consists of six phonon bands: three acoustic and three optical. Their frequencies can be experimentally determined using first-order Raman and Brillouin scattering only in the vicinity of the Γ point owing to the crystal momentum conservation. At Γ, the optical ($\omega_O = 1332$ cm^{-1}) and acoustic ($\omega_A = 0$ cm^{-1}) phonons are degenerate. Therefore, the first-order Raman spectrum of bulk diamond consists only of a single sharp band located at 1332 cm^{-1}.[39−42]

Clearly, the finite-size models considered here possess no translational symmetry and can be treated as very large molecules. Consequently, the Raman spectra of NDs can be expected to consist of a large number of bands corresponding to the Raman active vibrational modes. Their activities are, in principle, governed only by the T_d point group selection rules. In practice, however, it is reasonable to expect that, for large finite models, the vibrational densities of states (VDOSs) will resemble and in the limit of an infinite number of atoms will converge to the phonon density of states of the crystal diamond. This expected convergence behavior can be expressed alternatively by saying that the vibrational frequencies of large models studied here probe uniformly the phonon dispersion surfaces of diamond over the whole Brillouin zone. Therefore, it is reasonable to expect that the Raman activities of vibrational modes not corresponding to the Γ point (*i.e.*, out-of-phase with respect to the relative motion of unit cells inside the finite models) will contribute only marginally to the simulated Raman spectra. For smaller models, where the similarity is only approximate, the optical phonons at Γ would have a nonvanishing overlap with a larger number of vibrational modes of a finite model leading to the characteristic asymmetric line width broadening of the red-shifted zone-center mode and producing a number of additional Raman features. Note that this molecular interpretation is essentially equivalent to the phonon-confinement model[43] that was used previously to interpret the Raman spectra of nanocrystalline diamonds.[44] A similar interpretation can be given for the acoustic phonons that manifest themselves in finite models as a comb of low-frequency bands usually referred to as the cage deformation modes.

Speaking more precisely, it would be reasonable to expect the aforementioned behavior if we could avoid including the terminal hydrogen atoms in our model systems. The C−H stretching modes (2850−3400 cm^{-1}) are not interfering with the studied spectral region, but, unfortunately, the H−C−H bending modes (1350−1460 cm^{-1}) with *a priori* unpredictable intensity pattern do complicate the analysis of the simulated spectra. This complication is solved by setting the atomic mass of hydrogen to a large value (10 000 amu), which corresponds effectively to shifting away the intervening features from the studied spectral window. The Raman spectra obtained using this modification will be further referred to as the "infinitely heavy hydrogens" (briefly, infH) Raman spectra.

With the preceding theoretical considerations in mind, we are now ready to analyze the results of our simulations. As expected, the Raman spectra obtained for the hydrogen-terminated tetrahedral and octahedral finite models (shown in Figure 3) display a large number of active bands. Most of these bands have very small intensity. The bands are grouped in two families, one with $\omega < 400$ cm^{-1} and one centered around 1200 cm^{-1}. This pattern is more pronounced for larger NDs. The evolution of the simulated Raman signal with growing size of the models is very regular. The positions of the bands and their intensities change smoothly, demonstrating a clear convergence pattern underlying the Raman spectra of NDs. Two features of this evolution are worth particular attention. First, the number of intensive Raman bands is considerably reduced with the growing size of the model. For the largest model systems size of the tetrahedral family (T10), there are only seven intensive bands, while for that of the octahedral family (O8), almost all Raman intensity is carried by five bands. We use this regularity below to discuss the anticipated Raman spectra of much larger NDs, for which we could not afford explicit DFTB calculations. Second, the low-frequency bands experience a quite substantial red shift during the evolution, while the other bands (with $\omega > 800$ cm^{-1}) remain almost unchanged in the same region of the spectra for different size model systems. This feature allows for tracking back the origin of the active Raman bands of NDs to those of adamantane, which are much easier to interpret. A detailed analysis along this line is given below.

Evolution of the Low-Frequency Bands. The low-frequency bands originate from the breathing and cage-deformation modes and clearly can be associated with the acoustic phonons of diamond. Their frequencies and intensities converge rapidly with growing model size. For the largest studied models, O8 and T10, all of the low-frequency Raman bands are located below 200 cm^{-1}. The intensity and position pattern of these bands

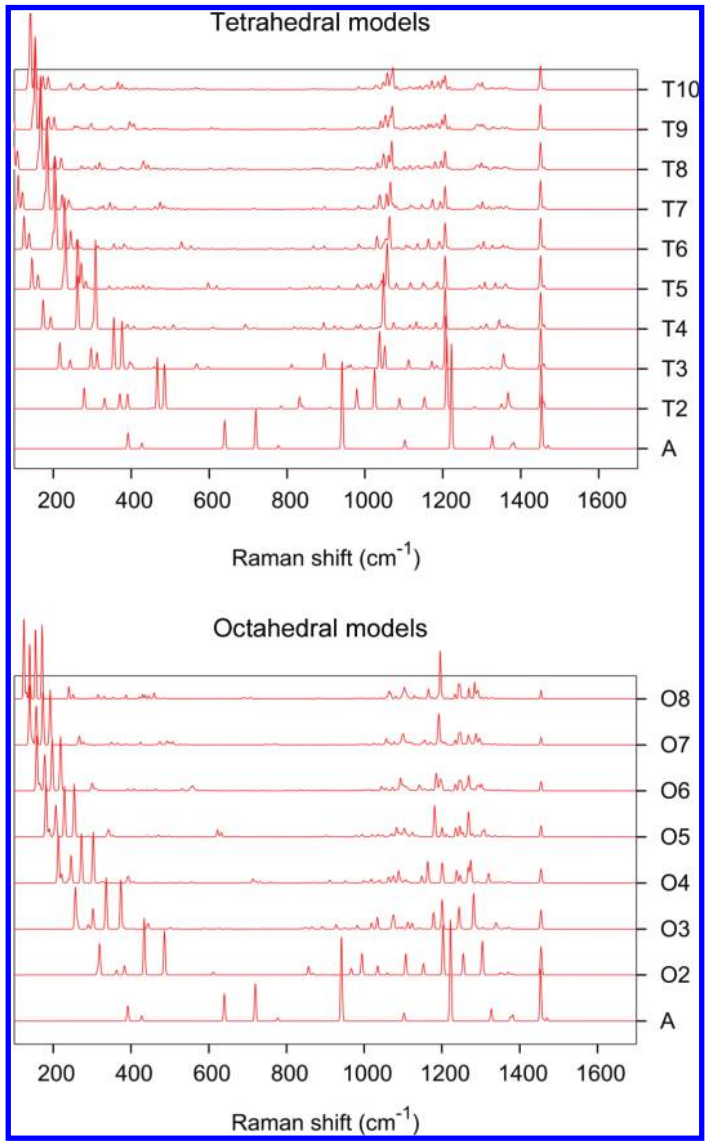

Figure 3. Evolution of the simulated Raman spectra for the tetrahedral and octahedral finite models of nanodiamonds.

is quite different for both studied families of structures. The octahedral models display a quartet of active bands, corresponding to the E, T_2, T_2, and A irreps, of approximately similar intensity. During evolution, the spacing between the peaks decreases and their frequencies approach zero. The tetrahedral models display two doublets of active bands, each of them showing similar behavior as discussed for the quartet of octahedral models. The active modes correspond to the following irreducible representations (irreps): E, T_2, E, T_2, and A; the second pair of the E and T_2 modes coincide, appearing as a single peak. Despite of the fact that the pattern is different for both families, it is clear that in the bulk limit of the size evolution they converge toward the same Rayleigh line. The strong dependence of the position of these peaks on the size of the model can be used as a diagnostic for determination of the size of the nanocrystalline grains of diamond, as suggested earlier by Filik *et al.*[28] We have fitted the positions of the observed bands to the following formula

$$\omega = an^{-b} \tag{2}$$

with n being the number of atoms in a given structure, using the data for the five largest models of each family. The quality of the fit is almost perfect (for details, see Supporting Information). Since the exponent b is roughly equal to 1/3, the low-frequency modes scale approximately inversely with the size of the model r_{max}. This behavior agrees well with the previous experimental semiconductor[45−47] and theoretical results.[48−50] To allow the prediction of the position of the low-frequency bands in general size nanocrystals, we give here the fitted coefficients for the limiting low-frequency bands of each model. They are $a = 882$ cm^{-1} and $b = 0.3691$ for the lowest band (E) and $a = 1410$ cm^{-1} and $b = 0.3431$ for the highest band (A) of the tetrahedral model, and $a = 1005$ cm^{-1} and $b = 0.3034$ for the lowest band (E) and $a = 1578$ cm^{-1} and $b = 0.3231$ for the highest band (A) of the octahedral model. Assuming that the regular pattern described here can be extrapolated also to much larger systems, eq 2 together with the given coefficients can be used to estimate the anticipated positions of the low-frequency bands in the recently reported Raman spectra of two single-crystal nanodiamonds.[23,24] The nanodiamond of the size 90 nm, which contains approximately 20 [10.5] million carbon atoms and corresponds effectively to a O246 [T314] model system, would have the low-frequency bands located in the range 5.7−6.9 [2.2−6.2] cm^{-1} assuming the octahedral [tetrahedral] regime. Analogously, the smaller nanodiamond of the size 35 nm, which contains approximately 1.2 [0.7] million carbon atoms and corresponds effectively to our O96 [T126] model, would have the low-frequency bands located in the range 14.0−17.2 [6.0−14.8] cm^{-1}. It would be relatively easy to distinguish between the two regimes, as the octahedral models display almost equally spaced bands, while for the tetrahedral models, the separation between the doublets becomes even more pronounced for large NDs. We note that eq 2 can be written as an analogue of the dependence of the radial breathing mode of single-walled carbon nanotubes on the inverse tube diameter[54]

$$\omega = an^{-b} \approx \frac{a'}{r_{max}} \tag{3}$$

where r_{max} takes the place of the tube diameter. We hope that these considerations can prove helpful for assessing the size and shape of diamond nanocrystals in low-frequency Raman spectroscopy experiments. We are aware that unfortunately, at present, the experimental sample quality for the size range of NDs, where these modes are detectable by Raman spectroscopy, does not allow detection of these features.

Evolution of the 800−1500 cm^{-1} Spectral Window. For the octahedral models, the bands located between 800 and 1500 cm^{-1} converge toward a single, dominant peak. DFTB predicts the position of this T_2 band, corresponding to the optical phonons of diamond, at approximately 1200 cm^{-1}. A detailed discussion of the evolution history for the T_2 band is given in the next section for both families of models. For the tetrahedral models, the convergence behavior is again quite different. The most important observation is that the models used by us are not sufficiently large to predict uniquely the Raman spectra of larger tetrahedral nanodiamonds. One may expect that the presented series of Raman spectra of T2−T10 would converge to three separated bands located around 1050, 1200, and 1450 cm^{-1}. In analogy with the octahedral models, the signal at 1200 cm^{-1} corresponds to the zone-center T_2 band. The remaining two bands, at 1050 and 1450 cm^{-1}, presumably fade away only for much larger numbers of atoms. Their origin can be easily traced back to specific vibrational modes of adamantane. The *E* band at 1450 cm^{-1}, whose position is practically constant for all models, originates from the 1453 cm^{-1} scissoring motion of the adamantane CH_2 groups (observed in experiment[51] at 1439 cm^{-1}). Clearly, there are very few reasons for this band to change its position during the evolution. Note that this band is present in all of the Raman spectra simulated by us, but for the octahedral models, it is rapidly shadowed by other, more intensive bands, while for the tetrahedral models, the decay of its relative intensity is much slower. The other mode, around 1050 cm^{-1}, evolves from the T_2 942 cm^{-1} vibration of adamantane (observed in experiment[51] at 970 cm^{-1}), which is a specific amalgam of CH_2 rocking, CC stretching, and CCC deformation. For larger models, the constituent contributions change slightly and the mode shifts toward higher frequencies: 1025 cm^{-1} for T2, 1038 cm^{-1} for T3, and 1048 cm^{-1} for T4.

Evolution of the T_2 Raman Band. The rate of convergence of the simulated Raman spectra of NDs can be most conveniently inspected by the analysis of the spectral region around 1100−1300 cm^{-1}, which effectively corresponds in DFTB to the optical phonons of diamond at Γ. The evolution of this region in the Raman spectra studied here of the three largest tetrahedral and octahedral structures is shown in Figure 4. For the octahedral structures, the convergence toward the diamond band is very clear and rapid. The intensity of the T_2 band is enhanced with the growing size of the model, while the intensity of the other bands is practically unaltered. The position of the T_2 band depends on the size of the model: 1185 cm^{-1} for O6, 1192 cm^{-1} for O7, and 1196 cm^{-1} for O8. (The corresponding diameters of these NDs are 2.2, 2.5, and 2.9 nm.) Unfortunately, our models are still too small to extrapolate this trend further as it has been done for the low-frequency modes. Such an extrapolation would allow us to evaluate how much the displaced position of the T_2 band in our simulation (∼1200 *vs* 1332 cm^{-1} in experiment) is caused by the harmonic approximation and the deficiencies of the DFTB method and how much it originates from the not fully converged size of our model. A certain estimation of this effect can be obtained by computing the DFTB vibrational frequencies for butane (C_4H_{10}) and comparing the position of the symmetric C↔C−C↔C stretch mode (982 cm^{-1}) with its experimental value (1059 cm^{-1}).[52] The difference of approximately 80 cm^{-1} suggests that in the DFTB Raman spectrum performed for a fully converged model one may expect the position of the T_2 band at approximately 1250 cm^{-1}. In this context, the red shift of the T_2 band by 50 cm^{-1} observed for small models is not surprising; an analogous effect was observed earlier in experiment[23,24] and in theory[17,44] when the size of the diamond nanocrystals was reduced from ∞ to 5.0 nm. We note in comparison that harmonic vibrational frequency calculations for bulk diamond using periodic boundary conditions predict the position of the T_2 anywhere between 1277 and 1361 cm^{-1}.[53]

The evolution pattern for the tetrahedral structures is much more structured. As can be seen from Figure 4, the Raman signal in the studied spectral window is actually dominated by an *E* band. The relative intensity of the T_2 band is slowly growing and may/will dominate the *E* band for much larger models than those inspected in the present study. The position of the T_2 band is gradually blue-shifted with the growing size of the model, analogously as for the octahedral models, while the position of the *E* band is practically uninfluenced.

Evolution of the Simulated infH Raman Spectra. It is easy to understand the difference between the Raman spectra of the tetrahedral and octahedral models taking into account the C/H ratio, closely related to the bulk/surface ratio for both the considered sets of models. The bulk/surface ratio (for an object with average side length *R*, volume scales with $R^3 \sim n$, and surface area scales with $\sim R^2$) naturally increases as a function of $n^{1/3}$ and linearly with the number of layers (which is directly proportional to *R*); however, for small model systems, deviations from ideal scaling are observed. Moreover, different polyhedra such as the octahedron and the tetrahedron possess different volume to surface ratios. This ratio is considerably smaller for the tetrahedral models, suggesting slower convergence of the corresponding Raman spectra patterns (for details, see Figures S1 and S2 in the Supporting Information). As mentioned earlier, a certain way to evade this problem is by artificially increasing the masses of the terminating hydrogen atoms in the mass-weighted Hessian matrix prior to diagonalization. Since the low-frequency modes are related to breathing and shearing, they are suppressed by this technique, and we are left only with the bands converging to the optical phonon of dia-

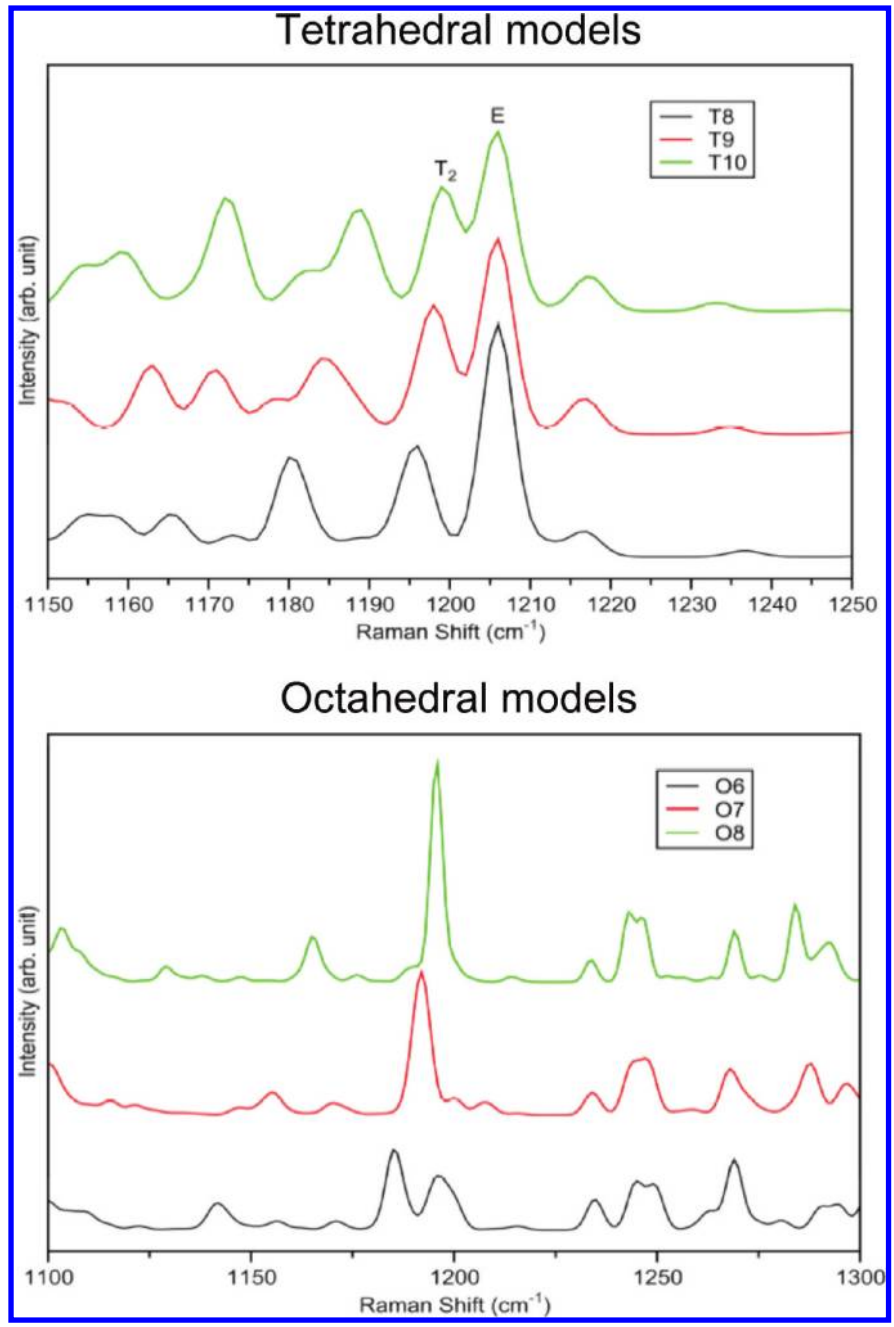

Figure 4. Evolution of the T_2 band in the simulated Raman spectra of the three largest tetrahedral (T8−T10) and octahedral (O6−O8) models of nanodiamonds.

mond. Consequently, the simulated infH Raman spectra simulated using only the T_2 modes (shown in Figure 5) are markedly simpler and consist only of a single group of peaks corresponding to the optical phonon of diamond. The evolution history and the final Raman pattern are quite similar for both families of NDs. For smaller models, a number of moderately intense peaks are observed. When the size of the models grow, these peaks merge together developing a single, dominating band centered at approximately 1200 cm^{-1}. The convergence toward the Raman spectrum of a diamond crystal is remarkably rapid. For the largest studied models, the only different spectral feature is a satellite band consisting of low-intensity peaks between 1250 and 1300 cm^{-1}. Clearly, as can be inferred from their evolution behavior, this band will vanish for larger finite models.

The details of the evolution history of the zone-center T_2 band for the simulated infH Raman spectra is presented in Figure 6 for both families of models. As mentioned earlier, the convergence is rapid. The resultant band consists of a number of closely spaced Raman signals; their number is substantially larger for the tetrahedral models. The half-width of the effective envelope of the Raman band is reduced with the growing size of the model; this effect is particularly pronounced

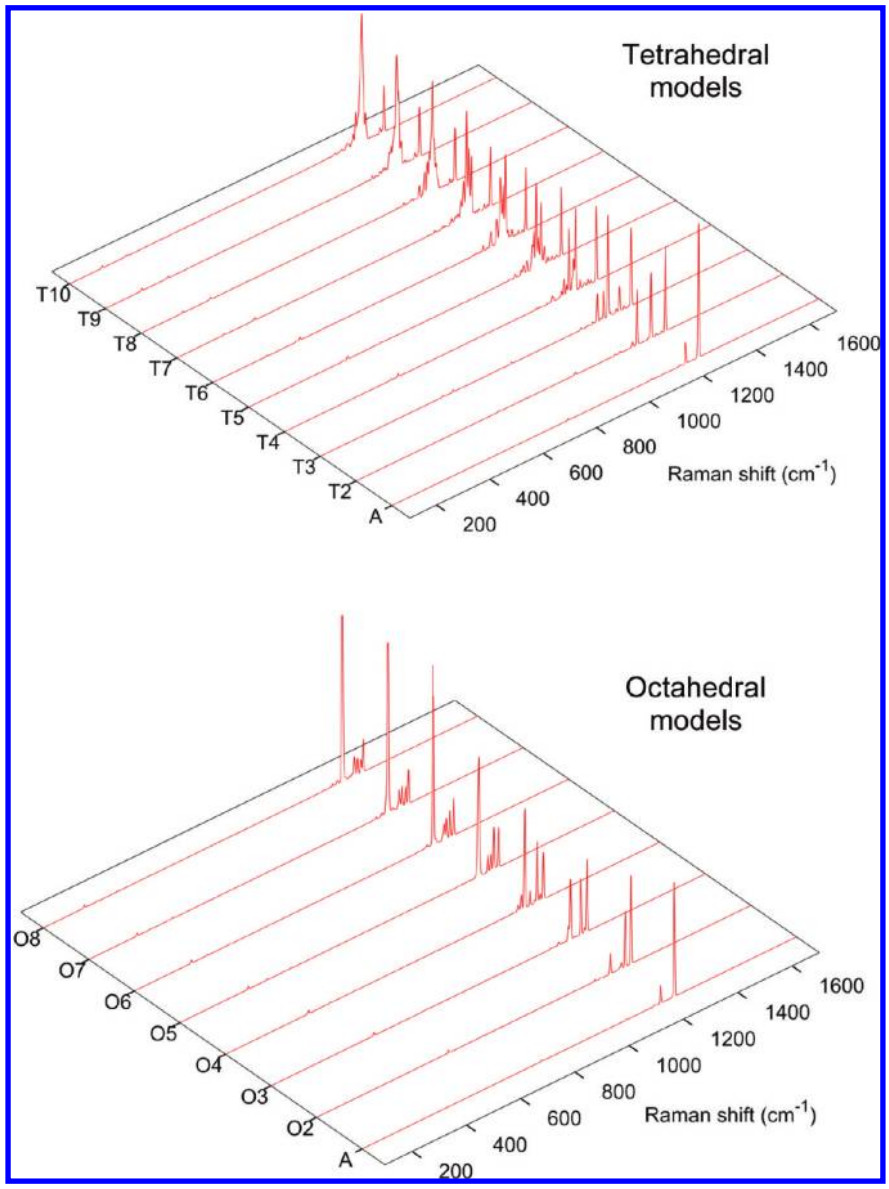

Figure 5. Evolution of the simulated infH Raman spectra for the tetrahedral and octahedral models of nanodiamonds. For details, see text.

for the tetrahedral NDs. Note that this observation is in line with the earlier theoretical and experimental results obtained for large nanodiamond crystals, where the position of the T_2 band and its half-width were shown to be closely related to the size of the ND grains (for comparison, see in particular Figure 8 of ref 44 and Figure 3 of ref 17).

SUMMARY AND CONCLUSIONS

The size evolution of the Raman spectra of octahedral and tetrahedral NDs with a diameter range of 0.3−2.9 nm has been studied using the DFT and DFTB methods. To the best of our knowledge, this is the first time that the size evolution of Raman spectra for molecules up to about 1000 atoms was followed using a quantum chemical method of similar accuracy to DFT. A clear and smooth convergence toward the Raman spectrum of a diamond crystal has been observed, particularly in the octahedral regime. The Raman spectrum of the largest studied octahedral structure, O8 ($C_{969}H_{324}$), is dominated by a single T_2 band at 1200 cm^{-1} corresponding to the optical phonons of diamond at Γ, and a comb of low-frequency bands located between 120 and 170 cm^{-1}, which correspond to the diamond's acoustic phonons. In the tetrahedral regime, two additional spectral features are detected, at 1050 and 1450 cm^{-1}, which we assume will fade away for model systems larger than those studied here since they originate from surface effects. This assumption is based on the fact that these features do not persist in the octahedral regime and, therefore, are expected to similarly fade away since the Raman spectra for both polyhedra types have to converge in the bulk limit. The position of the T_2 band for both families of structures is gradually blue-shifted with the growing size of the

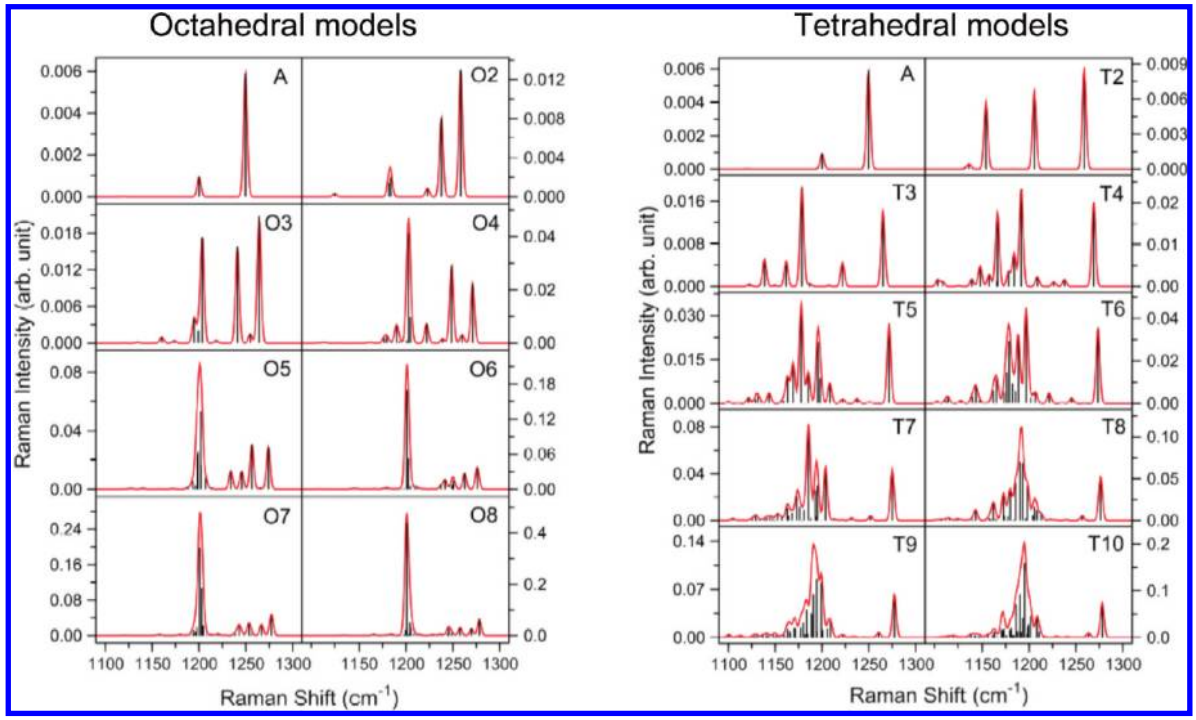

Figure 6. Formation of the T_2 band of diamond in the simulated infH Raman spectra of the octahedral and tetrahedral nanodiamonds.

model. This suggests that one of the reasons for the observed discrepancy between the positions of the simulated (~1200 cm^{-1}) and experimental (1325 to 1332 cm^{-1}) band—in addition to that of the harmonic approximation and the inherently approximate nature of DFTB—may be the insufficiently large size of the models studied here. This observation particularly applies to the family of tetrahedral structures, for which the convergent trend in the evolution of the non-low-frequency bands requires large model systems.

We obtained three important findings from this work. (i) We have given a quantitative relationship between the ND size and the position of the low-frequency Raman active peaks (eqs 2 and 3) as a an analogue of the dependence of the frequency of the radial breathing mode (RBM) on the inverse diameter in single-walled carbon nanotubes.[54] (ii) The Raman spectra evolution pattern depends quite strongly on the shape (here octahedral *versus* tetrahedral family) of the crystalline ND grains. To the best of our knowledge, the influence of the shape on the appearance of the ND Raman spectra has not been considered before. (iii) No evidence of other spectral features previously suggested for Raman characterization of ND samples is found in our simulations, in good agreement with previous considerations from experiments.[19,25] Our work confirms the theoretical predictions made by Filik *et al.*[28] that the only Raman activity expected for NDs is associated with the zone-center mode around 1325 cm^{-1} and the low-frequency cage deformation and breathing modes. Studies of the effect of defects, different and irregular shapes, and surface functional groups on ND vibrational spectra are currently ongoing in our laboratories.

METHODS

Density functional theory (DFT) calculations using BLYP/3-21G[55−57] and BLYP/6-31+G*[55,56,58−60] were performed using the implementation in the GAUSSIAN 03 quantum chemistry code with default convergence criteria.[61] BLYP is known to yield harmonic vibrational frequencies that are in better agreement with experiment than hybrid functionals such as B3LYP, which inherit the systematic error of the Hartree−Fock method. We computed equilibrium geometries, harmonic vibrational frequencies, and Raman activities following the standard procedures. SCC-DFTB calculations were performed using a standalone FORTRAN-based DFTB code with an implemented analytical Hessian module.[38,62,63] For geometric optimization of the nanodiamond (ND) models, we adopted the SCC energy convergence criterion of 10^{-12} hartree for energies and 10^{-6} for the gradient in atomic units. The Hessian and computed harmonic frequencies were left unscaled to allow for transferability of the reported data. The Raman intensities were obtained[38] from the computed activities assuming the following experimental conditions: T = 25 °C and λ_{laser} = 514.5 nm. The simulated DFT and DFTB Raman spectra were constructed by superposing Gaussians (with half-width of 1.5 cm^{-1}) located at the computed harmonic vibrational frequencies with heights corresponding to the calculated intensity. The presented Raman spectra are given in arbitrary intensity units; the area under each spectrum is normalized to unity.

It was found that the hydrogen-terminated surface of the investigated models produces a large number of spurious Raman peaks. In order to minimize this undesirable effect, the masses of the terminal hydrogen atoms were set to a very large value (10 000 amu) in analogy with previous work on polycyclic aro-

matic hydrocarbons (PAH)[64] and nanodiamonds.[28] This change effectively eliminates the surface contribution to the Raman spectra, allowing only the inner carbons to vibrate.

Acknowledgment. S.I. is grateful to Eiji Osawa for several profound discussions on nanodiamonds and related topics. We thank the National Center for High-Performance Computing of Taiwan for computer facilities. Financial support from National Science Council of Taiwan (NSC96-2113-M-009-022) and the ATU project of the Ministry of Education, Taiwan, is acknowledged. S.I. and W.L. acknowledge support by the Program for Improvement of Research Environment for Young Researchers from Special Coordination Funds for Promoting Science and Technology (SCF) commissioned by the Ministry of Education, Culture, Sports, Science and Technology (MEXT) of Japan.

Supporting Information Available: PDF file giving additional details of our simulations (equilibrium geometries, vibrational frequencies and intensities, fitting results, and additional graphs) is available online. This material is available free of charge *via* the Internet at http://pubs.acs.org.

REFERENCES AND NOTES

1. Lewis, R. S.; Tang, M.; Wecker, J. F.; Anders, E.; Steel, E. Interstellar Diamonds in Meteorites. *Nature* **1987**, *326*, 160–162.
2. Shenderova, O. A.; Zhirnov, V. V.; Brenner, D. W. Carbon Nanostructure. *Crit. Rev. Solid State Mater Sci.* **2002**, *27*, 227–356.
3. Greiner, N. R.; Phillips, D. S.; Johnson, J. D.; F.; Volk, A. Diamonds in Detonation Soot. *Nature* **1988**, *333*, 440–442.
4. Ashfold, M. N. R.; May, P. W.; Rego, C. A.; Everitt, N. M. Thin Film Diamond by Chemical Vapour Deposition Methods. *Chem. Soc. Rev.* **1994**, *23*, 21–30.
5. Shenderova, O. A.; Gruen, D. M. *Ultrananocrystalline Diamond: Synthesis, Properties, and Applications*; William Andrew: Norwich, NY, 2006; p600.
6. Shenderova, O.; Tyler, T.; Cunningham, G.; Ray, M.; Walsh, J.; Casulli, M.; Hens, S.; McGuire, G.; Kuznetsov, V.; Lipa, S. Nanodiamond and Onion-like Carbon Polymer Nanocomposites. *Diamond Relat. Mater.* **2007**, *16*, 1213–1217.
7. Dolmatov, V. Y. Detonation-Synthesis Nanodiamonds: Synthesis, Structure, Prosperities and Application. *Russ. Chem. Rev.* **2007**, *76*, 339–360.
8. Gibson, N.; Fitzgerald, Z.; Luo, T.-J.; Shenderova, O.; Grichko, V.; Bondar, V.; Puzyr, A.; Brenner, D. W. Nanodiamonds for Detoxification. *Nanotechnology* **2007**, *2*, 713–716.
9. Bondar, V. S.; Pozdnyakova, I. O.; Puzyr, A. P. Applications of Nanodiamonds for Separation and Purification of Proteins. *Phys. Solid State* **2004**, *46*, 758–760.
10. Ho, D. Beyond the Sparkle: The Impact of Nanodiamonds as Biolabeling and Therapeutic Agents. *ACS Nano* **2009**, *3*, 3825–3829.
11. Huang, H.; Pierstorff, E.; Osawa, E.; Ho, D. Active Nanodiamond Hydrogels for Chemotherapeutic Delivery. *Nano Lett.* **2007**, *7*, 3305–3314.
12. Zhang, X.-Q.; Chen, M.; Lam, R.; Xu, X.; Osawa, E.; Ho, D. Polymer-Functionalized Nanodiamond Platforms as Vehicles for Gene Delivery. *ACS Nano* **2009**, *3*, 2609–2616.
13. Maze, J. R.; Stanwix, P. L.; Hodges, J. S.; Hong, S.; Taylor, J. M.; Cappellaro, P.; Jiang, L.; Gurudev Dutt, M. V.; Togan, E.; Zibrov, A. S.; Yacoby, A.; Walsworth, R. L.; Lukin, M. D. Nanoscale Magnetic Sensing with an Individual Electronic Spin in Diamond. *Nature* **2008**, *455*, 644–647.
14. Balasubramanian, G.; Chan, I. Y.; Kolesov, R.; Al-Hmoud, M.; Tisler, J.; Shin, C.; Kim, C.; Wojcik, A.; Hemmer, P. R.; Krueger, A.; Hanke, T.; Leitenstorfer, A.; Bratschitsch, R.; Jelezko, F.; Wrachtrup, J. Nanoscale Imaging Magnetometry with Diamond Spins under Ambient Conditions. *Nature* **2008**, *455*, 648–651.
15. Nemanich, R. J.; Glass, J. T.; Lucovsky, G.; Shroder, R. E. Raman Scattering Characterization of Carbon Bonding in Diamond and Diamondlike Thin Films. *J. Vac. Sci. Technol., A* **1988**, *6*, 1783–1787.
16. Shroder, R. E.; Nemanich, R. J.; Glass, J. T. Analysis of the Composite Structures in Diamond Thin Films by Raman Spectroscopy. *Phys. Rev. B* **1990**, *41*, 3738–3745.
17. Yoshikawa, M.; Mori, Y.; Maegawa, M.; Katagiri, G.; Ishida, H.; Ishitani, A. Raman Scattering from Diamond Particles. *Appl. Phys. Lett.* **1993**, *62*, 3114–3116.
18. Prawer, S.; Nugent, K. W.; Jamieson, D. N.; Orwa, J. O.; Bursill, L. A.; Peng, J. L. The Raman Spectrum of Nanocrystalline Diamond. *Chem. Phys. Lett.* **2000**, *332*, 93–97.
19. Ferrari, A. C.; Robertson, J. Origin of the 1150 cm^{-1} Raman Mode in Nanocrystalline Diamond. *Phys. Rev. B* **2001**, *63*, 121405/1–121405/4.
20. Pfeiffer, R.; Kuzmany, H.; Salk, N.; Günther, B. Evidence for *trans*-Polyacetylene in Nanocrystalline Diamond Films from H-D Isotropic Substitution Experiments. *Appl. Phys. Lett.* **2003**, *82*, 4149–4150.
21. Ferrari, A. C.; Robertson, J. Raman Spectroscopy of Amorphous, Nanostructured, Diamond-like Carbon, and Nanodiamond. *Philos. Trans. R. Soc. London, Ser. A* **2004**, *362*, 2477–2512.
22. May, P. W.; Smith, J. A.; Rosser, K. N. 785 nm Raman Spectroscopy of CVD Diamond Films. *Diamond Relat. Mater.* **2008**, *17*, 199–203.
23. Sun, K. W.; Wang, J. Y.; Ko, T. Y. Photoluminescence and Raman Spectroscopy of Single Diamond Nanoparticle. *J. Nanopart. Res.* **2008**, *10*, 115–120.
24. Sun, K. W.; Wang, J. Y.; Ko, T. Y. Raman Spectroscopy of Single Nanodiamond: Phonon-Confinement Effects. *Appl. Phys. Lett.* **2008**, *92*, 153115/1.
25. Mochalin, V.; Osswald, S.; Gogotsi, Y. Contribution of Functional Groups to the Raman Spectrum of Nanodiamond Powders. *Chem. Mater.* **2009**, *21*, 273–279.
26. Qiao, Z.; Li, J.; Zhao, N.; Shi, C.; Nash, P. Structural Evolution and Raman Study of Nanocarbons from Diamond Nanoparticles. *Chem. Phys. Lett.* **2006**, *429*, 479–482.
27. Zhang, D.; Zhang, R. Q. Signature of Nanodiamond in Raman Spectra: A Density Functional Theoretical Study. *J. Phys. Chem. B* **2005**, *109*, 9006–9013.
28. Filik, J.; Harvey, J. N.; Allan, N. L.; May, P. W.; Dahl, J. E. P.; Liu, S.; Carlson, R. M. K. Raman Spectroscopy of Nanocrystalline Diamond: An *Ab Initio* Approach. *Phys. Rev. B* **2006**, *74*, 035423/1–035423/10.
29. Shen, M. Z.; Schaefer, H. F.; Liang, C. X.; Lii, J. H.; Allinger, N. L.; Schleyer, P. v. R. Finite T_d Symmetry Models for Diamond: From Adamantane to Super-Adamantane ($C_{35}H_{36}$). *J. Am. Chem. Soc.* **1992**, *114*, 497–505.
30. Elstner, M.; Porezag, D.; Jungnickel, G.; Elsner, J.; Haugk, M.; Frauenheim, T.; Suhai, S.; Seifert, G. Self-Consistent-Charge Density-Functional Tight-Binding Method for Simulations of Complex Materials Properties. *Phys. Rev. B* **1998**, *58*, 7260–7268.
31. Porezag, D.; Frauenheim, T.; Köhler, T.; Seifert, G.; Kaschner, R. Construction of Tight-Binding-like Potentials on the Basis of Density-Functional Theory: Application to Carbon. *Phys. Rev. B* **1995**, *51*, 12947–12957.
32. Witek, H. A; Morokuma, K. Systematic Study of Vibrational Frequencies Calculated with the Self-Consistent Charge Density Functional Tight-Binding Method. *J. Comput. Chem.* **2004**, *25*, 1858–1864.
33. Małolepsza, E.; Witek, H. A.; Morokuma, K. Accurate Vibrational Frequencies Using the Self-Consistent-Charge Density-Functional Tight-Binding Method. *Chem. Phys. Lett.* **2005**, *412*, 237–243.
34. Witek, H. A.; Irle, S.; Zheng, G.; de Jong, B.; Morokuma, K. Modeling Carbon Nanostructures with the Self-Consistent Charge Density-Functional Tight-Binding Method: Vibrational and Electronic Spectra of C_{28}, C_{60}, and C_{70}. *J. Chem. Phys.* **2006**, *125*, 214706/1–214706/15.
35. Małolepsza, E.; Witek, H. A.; Irle, S. Comparison of Geometric, Electronic, and Vibrational Properties of Small Fullerenes C_{20}-C_{36}. *J. Phys. Chem. A* **2007**, *111*, 6649–6657.

36. Witek, H. A.; Trzaskowski, B.; Małolepsza, E.; Morokuma, K.; Adamowicz, L. Computational Study of Molecular Properties of Aggregates of C_{60} and (16,0) Zigzag Nanotube. *Chem. Phys. Lett.* **2007**, *446*, 87–91.
37. Małolepsza, E.; Lee, Y. P.; Witek, H. A.; Irle, S.; Lin, C. F.; Hsieh, H. M. Comparison of Geometric, Electronic, and Vibrational Properties for All Pentagon/Hexagon-Bearing Isomers of Fullerenes C_{38}, C_{40}, and C_{42}. *Int. J. Quantum Chem.* **2009**, *109*, 1999–2011.
38. Witek, H. A.; Morokuma, K.; Stradomska, A. Modeling Vibrational Spectra Using the Self-Consistent Charge Density-Functional Tight-Binding Method. I. Raman Spectra. *J. Chem. Phys.* **2004**, *121*, 5171–5178.
39. Ramaswamy, C. Raman Effect in Diamond. *Nature* **1930**, *125*, 704.
40. Warren, J. L.; Yarnell, J. L.; Dolling, G.; Cowley, R. A. Lattice Dynamics of Diamond. *Phys. Rev.* **1966**, *158*, 805–808.
41. Solin, S. A.; Ramdas, A. K. Raman Spectrum of Diamond. *Phys. Rev. B* **1970**, *1*, 1687–1698.
42. Prawer, S.; Nemanich, R. J. Raman Spectroscopy of Diamond and Doped Diamond. *Philos. Trans. R. Soc. London, Ser. A* **2004**, *362*, 2537–2565.
43. Richter, H.; Wang, Z. P.; Ley, L. The One Phonon Raman Spectrum in Microcrystalline Silicon. *Solid State Commun.* **1981**, *39*, 625–629.
44. Ager III, J. W.; Veirs, D. K.; Rosenblatt, G. M. Spatially Resolved Raman Studies of Diamond Films Grown by Chemical Vapor Deposition. *Phys. Rev. B* **1991**, *43*, 6491–6499.
45. Ovsyuk, N. N.; Gorokhov, E. B.; Grishchenko, V. V.; Shebanin, A. P. Low-Frequency Raman Scattering by Small Semiconductor Particles. *JETP Lett.* **1988**, *47*, 298–302.
46. Tanaka, A.; Onari, S.; Arai, T. Low-Frequency Raman Scattering from CdS Microcrystals Embedded in a Germanium Dioxide Glass Matrix. *Phys. Rev. B* **1993**, *47*, 1237–1243.
47. Champagnon, B.; Andrianasolo, B.; Duval, E. Size Determination of Semiconductor Nanocrystallites in Glasses by Low Frequency Inelastic Scattering (LOFIS). *Mater. Sci. Eng. B* **1991**, *9*, 417–420.
48. Lamb, H. On the Vibrations of a Spherical Shell. *Proc. London Math. Soc.* **1882**, *13*, 50–56.
49. Cheng, W.; Ren, S. F.; Yu, P. Y. Theoretical Investigation of the Surface Vibrational Modes in Germanium Nanocrystals. *Phys. Rev. B* **2003**, *68*, 193309/1–193309/4.
50. Cheng, W.; Ren, S. F.; Yu, P. Y. Microscopic Theory of the Low Frequency Raman Modes in Germanium Nanocrystals. *Phys. Rev. B* **2005**, *71*, 174305/1–174305/10.
51. Bistričić, L.; Baranović, G.; Mlinarić-Majerski, K. A Vibrational Assignment of Adamantane and Some of Its Isotopomers. Empirical *versus* Scaled Semiempirical Force Field. *Spectrochim. Acta* **1995**, *51*, 1643–1664.
52. Shimanouchi, T. *Tables of Molecular Vibrational Frequencies*, NSRDS NBS-39 (1972).
53. Izmaylov, A. F.; Scuseria, G. E. Efficient Evaluation of Analytic Vibrational Frequencies in Hartree−Fock and Density Functional Theory for Periodic Nonconducting Systems. *J. Chem. Phys.* **2007**, *127*, 144106/1–144106/9.
54. Kukovecz, A.; Kramberger, C.; Georgakilas, V.; Prato, M.; Kuzmany, H. A Detailed Raman Study on Thin Single-Wall Carbon Nanotubes Prepared by the HiPCO Process. *Eur. Phys. J. B* **2002**, *28*, 223–230.
55. Becke, A. Density-Functional Exchange-Energy Approximation with Correct Asymptotic Behavior. *Phys. Rev. A* **1998**, *38*, 3098–3100.
56. Lee, C. Y.; Yang, W.; Parr, R. G. Development of the Colle-Salvetti Correlation-Energy Formula into a Functional of the Electron Density. *Phys. Rev. B* **1988**, *37*, 785–789.
57. Binkley, J. S.; Pople, J. A.; Hehre, W. J. Self-Consistent Molecular Orbital Methods. 21. Small Split-Valence Basis Sets for First-Row Elements. *J. Am. Chem. Soc.* **1980**, *102*, 939–947.
58. Hehre, W. J.; Ditchfield, R.; Pople, J. A. Self-Consistent Molecular Orbital Methods. XII. Further Extensions of Gaussian-Type Basis Sets for Use in Molecular Orbital Studies of Organic Molecules. *J. Chem. Phys.* **1972**, *56*, 2257–2261.
59. Hariharan, P. C.; Pople, J. A. The Influence of Polarization Functions on Molecular Orbital Hydrogenation Energies. *Theor. Chim. Acta* **1973**, *28*, 213–222.
60. Clark, T.; Chandrasekhar, J.; Spitznagel, G. W.; Schleyer, P. v. R. Efficient Diffuse Function-Augmented Basis Sets for Anion Calculations. III. The 3-21+G Basis Set for First-Row Elements, Li-F. *J. Comput. Chem.* **1983**, *4*, 294–301.
61. Frisch, M. J. *et al. Gaussian 03*, revision A.1; Gaussian, Inc.: Pittsburgh, PA, 2003.
62. Witek, H. A.; Irle, S.; Morokuma, K. Analytical Second-order Geometrical Energy Derivatives of the Self-Consistent-Charge Density-Functional Tight-Binding Method. *J. Chem. Phys.* **2004**, *121*, 5163–5170.
63. Witek, H. A.; Morokuma, K.; Stradomska, A. Modeling Vibrational Spectra Using the Self-Consistent Charge Density-Functional Tight-Binding Method II: Infrared Spectra. *J. Theor. Comput. Chem.* **2005**, *4*, 639–655.
64. Negri, F.; Castiglioni, C.; Tommasini, M.; Zerbi, G. A Computational Study of the Raman Spectra of Large Polycyclic Aromatic Hydrocarbons: Toward Molecularly Defined Subunits of Graphite. *J. Phys. Chem. A* **2002**, *106*, 3306–3317.